Journal of Magnetic Resonance **139,** 175–180 (1999)
Article ID jmre.1999.1741, available online at http://www.idealibrary.com on IDEAL®

COMMUNICATIONS

Novel Methods for Characterizing a Decoupler Channel Using "Undetectable" Quantum Coherences

M. Robin Bendall and Thomas E. Skinner*

*The Russell Grimwade School of Biochemistry and Molecular Biology, University of Melbourne, Parkville 3052, Victoria, Australia; and *Department of Physics, Wright State University, Dayton, Ohio 45435*

Received November 24, 1998; revised February 17, 1999

Exact solutions for the effect of time-independent RF pulses on any initial configuration of an IS *J*-coupled system demonstrate that on-resonance CW decoupling yields signals whose frequency depends on RF field strength and homogeneity. These signals are enhanced starting with "undetectable" antiphase and multiple quantum coherences, which can also produce centerband intensity to mimic the signal from decoupled S_x. Conversely, these coherences can be generated from S_x using a low-power pulse, $B_1 = J/2$, of length $(\sqrt{2}J)^{-1}$, dubbed a "90^J pulse" since it is the selective equivalent of $\{(2J)^{-1}–90[I]\}$. Utilizing 90^J pulses, new characterization-of-decoupler (COD) pulse sequences can determine the performance of an insensitive I-spin channel by observing large signals from either antiphase or multiple quantum coherences with the S-spin channel, allowing, in minutes rather than hours: (i) frequency calibration to an accuracy of 0.1 Hz; (ii) measurement of RF amplitudes over a 500-fold variation; and (iii) mapping of RF homogeneity along the sample axis with a single 1D B_1 spectrum. These 90^J coherence transfer pulses are of potential general use for selective spectroscopy.

Key Words: **decoupler calibration; coherence sidebands; RF inhomogeneity; 90^J pulse; selective NMR.**

Contrary to prevailing expectation (*1*), in a coupled IS spin system, the states $2S_yI_j$ ($j = x$, y, or z), produce observable signals, including centerband signals, during a 1D decoupled acquisition. Ironically, the decoupler field establishes an additional means of communication between I and S which yields a *J*-coupled evolution to directly detectable magnetization, S_x. For example, in adiabatic decoupling, these signals are evident as large and inconvenient "coherence sidebands" that must be eliminated (*2*). This paper presents a shift in viewpoint to consider useful applications of these signals. We have applied a vector picture of *J*-coupling during RF irradiation (*3, 4*) to CW decoupling, and for comparison we have calculated exact analytic quantum solutions for all possible initial conditions of an IS system. Part of this study, presented here, yields several efficient methods for characterizing the RF power and homogeneity of an Insensitive I-spin channel by observing large coherence signals with the Sensitive S-spin channel.

Over the past 4 decades, popular methods for the RF power calibration of a decoupler channel have developed in three stages. The earliest (*5, 6*) are derived from a solution for the off-resonance CW-decoupled signal starting with pure in-phase magnetization S_x (*7*), but these CW methods are unsuitable at high RF power because of the likelihood of damage from overheating the probe or sample. Consequently, the advent of pulsed NMR required second-stage methods in which the length of pulses applied to the unobserved nucleus were measured. The first and simplest pulse sequence for this purpose, $90[S]–(2J)^{-1}–\theta[I]$; acquire$[S]$, functions by adjusting the θ pulse angle to 90° to obtain a S/N null when $2S_yI_z$ is completely transformed to the $2S_yI_y$ state (*8*). The technique was republished in greater detail and extended several times thereafter (*9*). A third category of current methods, independently adopted by many laboratories, takes advantage of the increased reliability of modern hardware. Practitioners commonly calibrate their favorite pulse sequences, even very complex sequences, on all spectrometer channels by incrementation of single on-resonance pulses, which are ideally 90° in normal use, to obtain S/N nulls when the pulses are close to 180°. The novel ideas described here are not intended to replace this 180°/null technique at high RF power. However, at low power, complications arise from pulse lengths being a significant fraction of $1/J$, and off-resonance effects become critical. Furthermore, the trial-and-error search for a S/N null is difficult to automate and so takes hours to calibrate 20 or more RF amplitudes. The new methods utilize these low-power effects and are readily automated to obtain numerous B_1 calibrations in a few minutes.

The homogeneity of RF fields is normally imaged using pulsed field gradients (see Ref. (*10*) for a brief review). Our new methods provide 1D acquisitions, without gradients, in which the sensitive S-spin signal is distributed across the frequency spectrum as a function of the I-spin RF amplitude.

1090-7807/99 $30.00

This provides valuable information on comparative homogeneity with a substantial increase in S/N. Small differences between probes are readily apparent. Spatial dimensions may be added to provide alternatives to the standard imaging methods.

For an IS spin system, solutions for the observable S_x component, ρ_{S_x}, of the density operator, $\rho(t)$, during arbitrary RF irradiation of I, have been published for the initial conditions $\rho(0) = S_x$ (*2, 11*) and $\rho(0) = 2S_yI_j$ [$j = x$, y, or z] (*2*). We have also derived solutions for these $2S_yI_j$ components, $\rho_{2S_yI_j}$. For CW irradiation (a square I pulse of any length, t), the resulting exact analytical expressions involve effective fields, $B_e^{\pm} = [B_1^2 + (\Delta H \pm J/2)^2]^{0.5}$, where ΔH is the resonance offset. For example, after a 90[S] pulse ($\rho(0) = S_x$), CW decoupling produces (see also Ref. (*7*))

$$\rho_{S_x}(t) = 0.5\{1 + (B_1^2 + \Delta H^2 - (J/2)^2)/(B_e^+B_e^-)\} \times \cos[\pi(B_e^+ - B_e^-)t] + 0.5\{1 - (B_1^2 + \Delta H^2 - (J/2)^2)/(B_e^+B_e^-)\}\cos[\pi(B_e^+ + B_e^-)t]. \quad [1]$$

For on-resonance ($\Delta H = 0$) CW decoupling, Eq. [1], and the new equations relevant here, simplify greatly in terms of $B_e^J = [B_1^2 + (J/2)^2]^{0.5}$ to

$$\rho(0) = S_x, \quad \rho_{S_x}(t) = \left(\frac{B_1}{B_e^J}\right)^2 + \left(\frac{J}{2B_e^J}\right)^2 \cos[2\pi B_e^J t]; \quad [2]$$

$$\rho(0) = S_x, \quad \rho_{2S_yI_y}(t) = -\frac{B_1}{B_e^J}\frac{J}{2B_e^J}(1 - \cos[2\pi B_e^J t]); \quad [3]$$

$$\rho(0) = 2S_yI_y, \quad \rho_{S_x}(t) = -\frac{B_1}{B_e^J}\frac{J}{2B_e^J}(1 - \cos[2\pi B_e^J t]); \quad [4]$$

$$\rho(0) = 2S_yI_z, \quad \rho_{S_x}(t) = \frac{J}{2B_e^J}\sin[2\pi B_e^J t]. \quad [5]$$

Note that Eqs. [4] and [5] describe the observable signal resulting from decoupling multiple quantum and antiphase coherences, despite the general assumption that no detectable signal is generated.

The residual splitting of the centerband, used in the original calibration methods (*5, 6*), is equal to $B_e^+ - B_e^-$, from the first term in Eq. [1]. It vanishes on resonance, generating Eq. [2] and a simple means of measuring both RF field strength and homogeneity. The FT of a FID described by Eq. [2] will yield a centerband with amplitude, $(B_1/B_e^J)^2$, and sidebands at $\pm B_e^J$ with amplitude $0.5(J/[2B_e^J])^2$. B_1 can be determined from the frequency difference between these sidebands, and their width depends on RF homogeneity.

Although these sidebands correspond to "lines 5" in Figs. 1a and 1b of Ref. (*7*), they were probably not used for the earliest means of calibration because they are weak for $B_1 \gg J$, FT NMR and ^{13}C labels were not available to enhance S/N, and these signals may have been broadened considerably by poorer RF homogeneity within earlier NMR coils. A literature search shows that later, with FT NMR, Simova (*12*) recognized the utility of the second term in Eq. [1], but did not take advantage of the simplification available on resonance (Eq. [2]). Moreover, Simova calibrated a dedicated ^{1}H decoupler channel via detection of the coupled ^{13}C signal. Multiple broadbanded channels, which can be used as observe or decoupler channels, are now common so ^{1}H power levels can be calibrated directly via the ^{1}H signal. In this study we emphasize the S/N gain in calibrating an insensitive I-spin channel (e.g., ^{13}C) via a sensitive S-spin channel (e.g., ^{1}H).

Comparison of the second terms of Eqs. [1] and [2] indicates that the sidebands in question have greater S/N for on-resonance decoupling. A more significant gain can be obtained by applying decoupling to multiple quantum coherence since a comparison of Eqs. [2] and [4] shows that the equivalent sidebands from $2S_yI_y$ are larger than those originating from S_x for all $B_1 > J/2$. Alternatively, the antiphase sidebands resulting from decoupling $2S_yI_z$ coherence (Eq. [5]) may be utilized if necessary because these are larger than those from $2S_yI_y$ for $B_1 \leq J/2$.

The $2S_yI_y$ spin state can be prepared in various ways, e.g., by the pulse sequence elements, 90[S]–$(2J)^{-1}$–90[I], but a more direct selective means can be synthesised from Eq. [3] when $B_1 = J/2$:

$$\rho(0) = S_x, \quad \rho_{2S_yI_y}(t) = -0.5(1 - \cos[2\pi B_e^J t]) = -\sin^2[\pi B_e^J t]. \quad [6]$$

Thus, when CW irradiation is applied on resonance with amplitude $B_1 = J/2$ for a discrete time, $t = (2B_e^J)^{-1} = (\sqrt{2}J)^{-1}$, S_x is completely transformed to $2S_yI_y$. This long RF pulse on the I spins is the selective equivalent of the pulse sequence elements, $(2J)^{-1}$–90[I], so it can be considered to be a special 90° pulse which we will now write as 90^J. We have been able to follow the concurrent evolution of the I- and S-spin states by experiment at intermediate stages throughout a 90^J pulse and so prove the identity in Eq. [6]. During the irradiation, via a complex time-dependent J-coupling mechanism, vectors representing the I-spin states are transformed from being effectively antiparallel along z to antiparallel along y, and this is concurrent with the S spins evolving from in-phase along x to antiparallel along y. The extensive detail of this research properly belongs in a subsequent full paper.

Taking Eqs. [2–6] together we identify a family of Characterization-Of-Decoupler (COD) pulse sequences:

$$90[S];\ \{\text{obs}[S],\ \text{CW}[I]\}, \quad [\text{COD1}]$$

$$90[S];\ 90^J[I_{+-}];\ \{\text{obs}[S_{+-}],\ \text{CW}[I]\}, \quad [\text{COD2}]$$

$$90[S];\ 90^J[I_{+-}];\ 90[I];\ \{\text{obs}[S_{+-}],\ \text{CW}[I]\}, \quad [\text{COD3}]$$

$$90_y[S];\ 90^J[I_{+-}];\ 90[S_{++--}];\ \{\text{obs}[I_{+---}],\ \text{CW}[S]\}, \quad [\text{COD4}]$$

$$90_y[S_{++--}];\ 90^J[I_{+-}];\ \{\text{obs}[I_{+---}],\ \text{CW}[S]\}. \quad [\text{COD5}]$$

All pulses and decoupling irradiation are on resonance, and they are of x phase unless specified. The notation, {obs[S], CW[I]}, signifies detection of the S spins while CW decoupling the I spins. The $\pm$ signs in COD2 and COD3 indicate concurrent alternation of pulse and receiver phase to eliminate all states except $2S_yI_y$. The extra 90[I] pulse in COD3 converts $2S_yI_y$ to $2S_yI_z$. Alternatively, COD4 and COD5 are the S-spin equivalents of COD3 and COD2, respectively, and can be used for characterization of the S-spin channel via decoupling $2I_yS_z$ and $2I_yS_y$, respectively. Note the 90° phase shift for the initial 90[S] pulses (typical of polarization transfer sequences) and a four-phase cycle is preferable as written.

COD1 is not novel. It is common to use a $^{13}CH_3$ group with COD1 to obtain an approximate on-resonance condition for the ^{13}C spins, but the simplicity of Eq. [2] for an IS-spin system may not be well appreciated. Since there is no residual splitting of the centerband on resonance at any power level, for an IS system the centerband will always increase in intensity as CW decoupling passes through zero offset for the I spins, independently of decoupling power—the equivalent situation for an IS_n moiety ($n > 1$) is more complex (*7*). This simplicity for an IS group is also manifested in Eqs. [3–6] and, in addition to better S/N than COD1, the COD2 and COD3 sequences eliminate uncoupled S signals (e.g., ^1H signals from $^{12}C^1H_n$ groups). Hence, our study is restricted to IS systems (e.g., ^{13}C-labeled formate) and COD1 should only be used to obtain approximate initial calibrations for the 90^J pulse and the I frequency as follows.

Without any initial assumptions, the I frequency can be roughly estimated using COD1 by finding when the residual splitting is minimized and thus the centerband maximized. Initially, B_1 may be set at 1 kHz or more with the transmitter frequency varied in increments of a kilohertz. When the I frequency has been located with an accuracy of $\pm 1/2$ kHz, these increments can be decreased by a factor of 10 and the B_1 amplitude should also be reduced by 10 dB. After a further reduction of 10 in increments and 10 dB in B_1, the I frequency will be known to within $\pm$5Hz and the sidebands at $\pm B_e^J$ should be obvious. If the identity of the sidebands is uncertain because B_1 was too large to begin with, or because of broadening from bad RF homogeneity or overlap with other resonances, B_1 can be repeatedly decremented by 10 dB until the centerband loses intensity and the sidebands approach $\pm J/2$ as $B_1 \rightarrow 0$. At this point B_1 should be increased in steps of 1 or 2 dB until the sidebands are at about $\pm J/\sqrt{2}$ as this provides the $B_1 = J/2$ calibration for the 90^J pulse. These calibrations are not critical since the frequency and amplitude for the 90^J pulse need only be accurate to $\pm J/10$ Hz and ± 1 dB, respectively, to obtain more than 90% of optimum signal intensity when using COD2 and COD3.

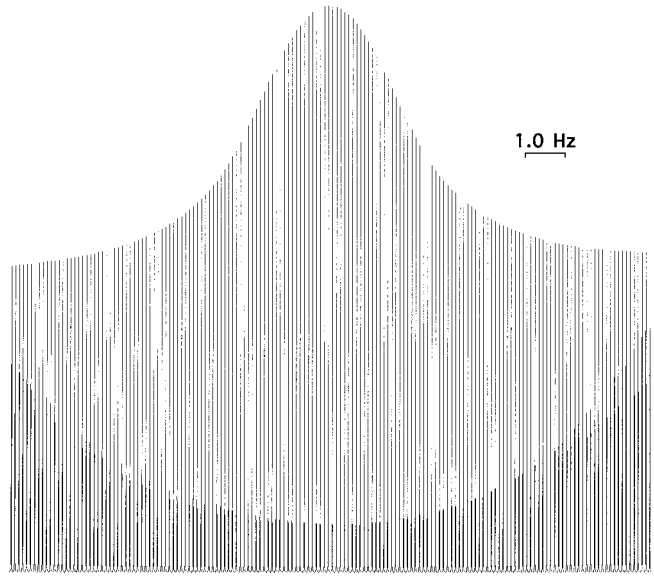

FIG. 1. RF frequency calibration of the I-spin decoupler channel. The large centerband signal obtained from applying low-power CW decoupling to $2S_yI_y$ coherence using the COD2 pulse sequence ($I \equiv {}^{13}C$, $S \equiv {}^1H$) is plotted as a function of frequency offset in 0.1-Hz intervals ($B_1 = 95$ Hz, corresponding to an attenuator setting of 10 dB in Fig. 2). The centerband is maximized on resonance, providing fast and precise calibration for the frequency of the I-spin channel via better S/N from the S spins. By contrast, frequency calibrations obtained by decoupling S_x using COD1 are not as accurate, because COD1 provides an asymmetric distribution of centerband amplitude resulting from the overlap of one line of the symmetric off-resonance doublet with the small isotopically shifted resonance from ^{12}C-formate—this provides a distribution which could also be mistakenly attributed to more than one frequency generated by the spectrometer's synthesiser. Experimental data for all the figures were obtained on a Varian INOVA-600 spectrometer, equipped with a 5-mm HCN triple-resonance PFG probe, using a 4% sample of ^{13}C(99.5%)–formate ($J = 194.6$ Hz) in D_2O containing a trace of gadolinium chloride to provide a ^1H linewidth of 3.5 Hz at 30°C.

If a more accurate value of the I-spin centerband frequency is required, it can be set on resonance to within 0.1 Hz or better using COD2. Potentially, the precision of the measurement increases with decreasing CW power because the envelope of the decoupled S-spin peak, plotted in Fig. 1, covers a smaller frequency range as a result of increased residual splitting at a given offset as B_1 decreases. However, Eq. [4] shows that the maximum centerband amplitude rapidly decreases for $B_1 < J/2$, which limits the ultimate precision obtainable. As described in the legend to Fig. 1, the same accuracy cannot be achieved with COD1 in those cases when the I spin is a partially enriched isotope such as the 99.5% ^{13}C–formate sample used here. This is a first example of the value of the selective nature of COD2 and COD3 (which also makes the B_e^J sidebands easy to observe even when they are very weak). Provided peak shapes are symmetric (good magnetic field homogeneity), studies of the kind shown in Fig. 1 also confirm

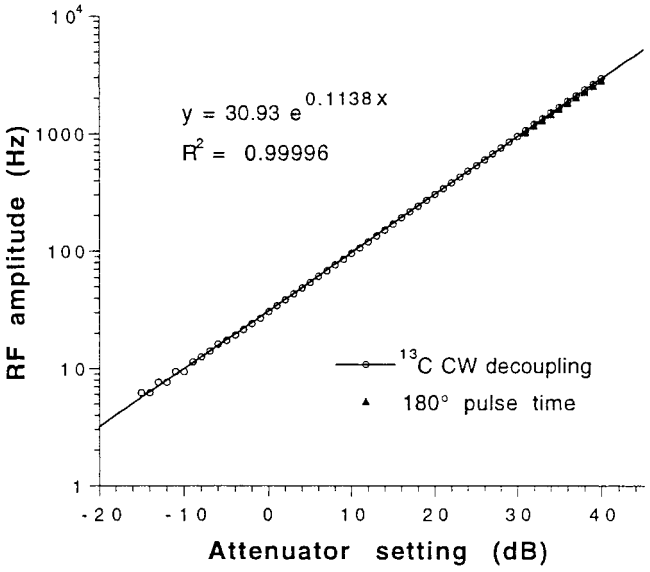

FIG. 2. RF amplitude calibration of the I-spin decoupler channel. Large satellite lines are produced at $\pm B_e^J$ relative to the centerband signal when low-power CW decoupling is applied on-resonance to $2S_yI_y$ coherence using the COD2 pulse sequence. RF fields calculated from the relation $B_1 = [(B_e^J)^2 - (J/2)^2]^{1/2}$, are plotted as a function of the spectrometer's coarse RF attenuator over a range of 55 dB in 1-dB increments. The lines at $\pm B_e^J$ are broadened by RF inhomogeneity, as discussed in more detail in Fig. 3. The frequency of the sidebands was determined as the midpoint of the top third of the broadened peaks to correspond to the dominant sensitive volume in the sample. This "average" frequency bisects the notch at the top of the sideband peaks (as displayed in Fig. 3) and bisects the top of the peak when this notch was not resolved at lower decoupling power. The "zig-zag" scatter seen in the last few points at low RF was produced by the limiting digital resolution defining the top of these peaks. For comparison with the more common 180°/null methods, RF amplitudes were also measured using COD3 by finding a S/N null when the 90[I] pulse was changed to 180° for the 10 attenuator settings from 31 to 40 dB. This method was used only at the high-power end of the scale to minimize effects of J coupling during long low-power pulses. These values are plotted as filled triangles, partially overlapping (and differing by 3% from) the points obtained by the CW decoupling method. This small difference is attributable to the $\theta\sin^n\theta\sin^m\phi$ signal dependence from each sample voxel which weights the B_1 field distribution for any method of measuring an average RF amplitude (discussed in the text in relation to Fig. 3), and from the uncertainty in estimating this weighted average from the broadened sidebands as described in the legend above.

that the second-channel frequency synthesiser is providing a single narrowband frequency.

Equation [4] shows that COD2 provides inverted $\pm B_e^J$ sidebands relative to the centerband and these yield a direct measurement of B_1 as demonstrated in Fig. 2. Thus COD2 gives a value of B_1 from every spectrum and so is easily automated to quickly provide a calibration curve over a large range of RF amplitudes. COD3 yields identical RF power data from antiphase sidebands (Eq. [5]), but has better S/N for $B_1 \leq J/2$. The techniques fail at high power where the sideband amplitudes, proportional to $J/(2B_e^J)$, are too small. However, heating from CW irradiation is a danger at high power and it will be usual to continue to calibrate high-power pulses at single B_1 settings by the 180°/null method. The accuracy of the new methods is demonstrated in Fig. 2 in comparison with results from the 180°/null method. Thus the new procedure is complementary to the old, enabling rapid calibrations at the lower power settings suitable for selective NMR and decoupling. Figure 2 illustrates that this technique can be used to determine whether the spectrometer's attenuators, amplifiers, and probes are indeed linear.

The frequency distribution of the B_e^J satellite lines produced in a simple 1D acquisition by any of the COD sequences can be used to quickly observe the homogeneity of the I-spin irradiation during on-resonance CW decoupling, since the frequency depends on B_1 amplitude. The average power level of the decoupling field should be high enough so that RF inhomogeneity dominates magnetic field inhomogeneity, but not so high as to produce poor S/N in the B_e^J lines. Again, care must be taken for COD1 that the sidebands do not overlap other small resonances, whereas COD2 and COD3 have the advantages of being selective and giving better S/N for the satellite lines. Typical spectra from COD1 and COD2, plotted in Fig. 3, show a split peak for the sidebands at $\pm B_e^J$, indicating a double peak in the RF amplitude produced by the coil. The lines are further broadened in the direction of the centerband showing a distribution of B_1 in the sample down to small values.

Differences in the spectra in Fig. 3 for offsets just outside $\pm J/2$ can be attributed to differences in the signal amplitude response from the pulse sequences that were used. For the 90[S];{observe S} elements of COD1, the signal from each sample voxel is proportional to $\theta\sin\theta$ (*13*), where θ is the spatially inhomogeneous pulse angle applied to the S spins in each voxel. In regions of the sample where B_1 is small enough that B_e^J is only a little larger than $J/2$, sideband amplitudes for COD2 are further reduced by the fraction of S_x converted to $2S_yI_y$ via the $\sin^2\phi$ expression in Eq. [6], where $\phi = \pi B_e^J t$. The signal for COD2 is thus proportional to $\theta\sin\theta\sin^2\phi$, which accounts for the differences between the sidebands in Figs. 3a and 3c. Although ϕ is given by the B_e^J sideband frequency axis, θ is unknown in the absence of further experiments.

For values greater than $\pm J/2$ relative to the centerband, the frequency axis can also be displayed directly as a B_1 axis as for Fig. 3c. Thus, although S/N is ambiguous because of the unknown θ pulse angle applied to the S spins, the frequency response is not. The simple experiment in Fig. 3a shows that RF inhomogeneity of the I-spin irradiation is sufficient to produce a continuous spectrum of B_1 down to zero units. But the RF homogeneity of the I coil cannot be expected to be good in sample regions outside the boundaries of the coil (where the S coil also has poor homogeneity). Adding a phase-cycled 180[S] pulse to COD1 after the 90[S] pulse converts the voxel response to $\theta\sin^3\theta$ (*13*). In Fig. 3b this converts the COD1 spectrum to one similar to COD2 as in Fig. 3c, which implies $\sin^2\theta \approx \sin^2\phi$ outside the coils where RF amplitudes are small. This suggests that the more homogeneous regions of the S and I coils are matched as they should be (confirmed in Fig. 4).

The addition of the 180[S] pulse demonstrates that the 90[S] pulse in COD sequences can be replaced by a pulse sequence of any length that produces S_x, thus enabling an estimation of the effect of I-spin RF inhomogeneity on any pulse sequence. As illustrated for the sequence in Fig. 3b, S/N is modified by an additional trigonometric term for each pulse (*14*). The effect of inhomogeneity will therefore decrease with an increased number of pulses since the B_1 field distribution is

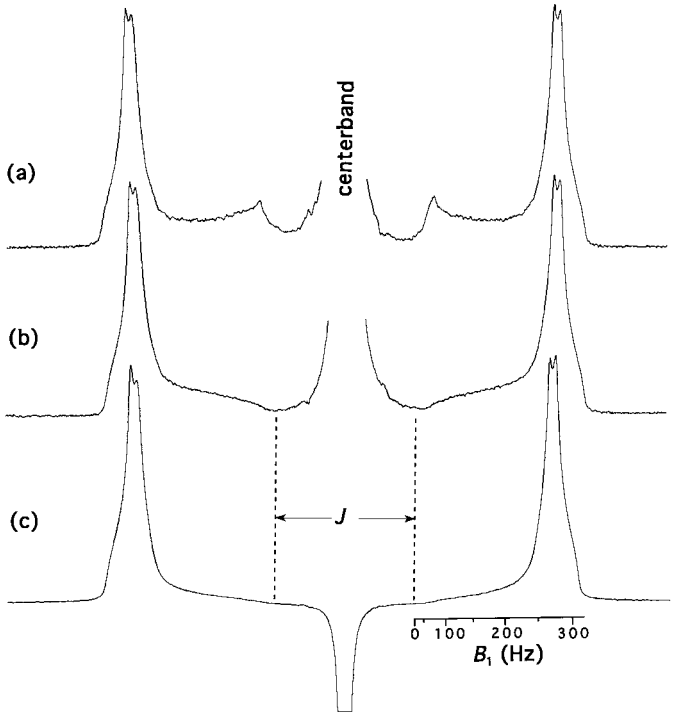

FIG. 3. RF inhomogeneity of the I-spin decoupler channel. The lines at $\pm B_e^J$ generated by the COD sequences are distributed over a range of frequencies by RF inhomogeneity, as illustrated in simple 1D spectra obtained using (a) COD1; (b) COD1 with a 180[$S_{\pm x \pm y}$] pulse prior to signal acquisition and receiver phase alternated as $+--+$; and (c) COD2. Sideband signal intensity begins at $\pm J/2$ relative to zero centerband frequency and extends to the left and right as given by $B_e^J = [B_1^2 + (J/2)^2]^{1/2}$, where B_1 is the spatially variable (inhomogeneous) RF field of the CW I-spin irradiation in the sample. The B_1 scale derived from this relation, applicable to all three spectra, is provided in (c). An anomalous probe having two dominant B_1 values for the ^{13}C coil, as illustrated by the dip at the top of the sideband peaks, was chosen for this paper to more clearly demonstrate RF inhomogeneity. A spectral width of 1000 Hz is displayed, with $B_1 = 270$ Hz for the I-spin CW irradiation (corresponding to an attenuator setting of 19 dB in Fig. 2). Spectra for COD1 and COD2 are defined by Eqs. [2] and [4], respectively. The COD2 spectrum in (c) has been inverted relative to COD1 in (a) and (b). At their maximum amplitude, the S/N for COD1/COD2 sidebands are in the ratio 0.06:0.17 as a fraction of unit S_x, and the centerbands are in the ratio $0.87{:}-0.34$. The baseline is distorted for all three spectra close to $\pm J/2$ because of the proximity of the intense centerband. Although sample regions outside the boundaries of the RF coil, where B_1 approaches zero ($\pm J/2$ in the spectra), are of little potential interest, they can nonetheless be detected with greater confidence by eliminating the centerband and this baseline ambiguity with COD3. The large centerband signal in (c), produced from $2S_yI_y$ coherence by on-resonance CW irradiation, illustrates the unanticipated nature of these coherence signals.

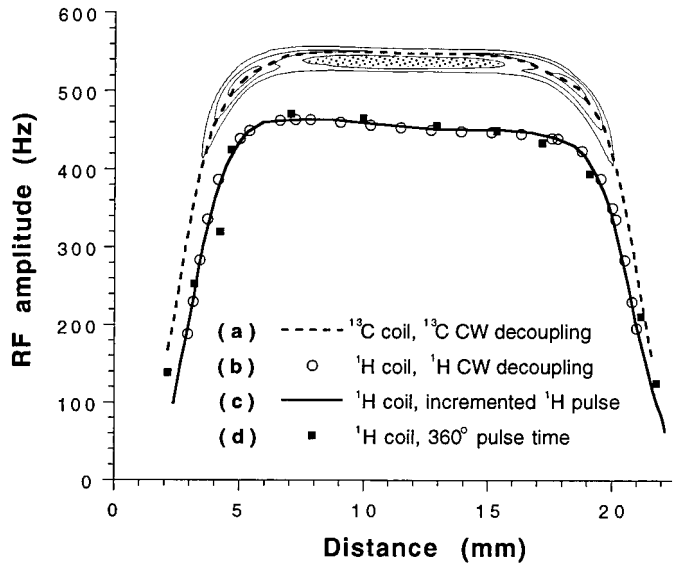

FIG. 4. Profiles of RF amplitude along the sample axis. 2D images of sideband signal intensity as a function of frequency, B_e^J, and of distance along the z axis of a 5-mm-diameter sample were obtained by inserting z-axis phase-encoding gradients in COD pulse sequences. The B_e^J axis was converted to RF amplitude using $B_1 = [(B_e^J)^2 - (J/2)^2]^{1/2}$. (a) A partial selection of signal contours is displayed and these were obtained for the ^{13}C coil using COD2 (^{13}C CW irradiation corresponding to an attenuator setting of 25 dB in Fig. 2) with a phase-encoding gradient inserted after the 90[S] pulse. Identical contours were obtained using COD3. The ellipsoidal central contour surrounds a region of lower signal intensity (dotted), which is revealed as the RF anomaly that produced the dip in the peaks of Fig. 3. The RF profile is represented as a simple line plot (dashed line) along the contour of maximum S/N at each point along the coil axis. (b) RF profile obtained for the ^{1}H coil using COD4 with a z-axis phase-encoding gradient on the I spin (^{13}C) inserted just prior to signal acquisition. (c) RF profile obtained for the ^{1}H coil using an incremented excitation pulse to provide the B_1 dimension and a read gradient to give the spatial dimension in the 2D image, according to Ref. (*10*). (d) RF profile obtained by Jahnke (*15*) by direct measurement of the RF field (360° pulse time, field gradients not used) for a similar ^{1}H coil by the same manufacturer. The B_1 axis for Jahnke's results has been scaled down to match the measurements in (b) and (c) obtained at lower RF field.

effectively narrowed from the product of $\theta \sin^n\theta$ and $\sin^m\phi$ terms originating from pulses on the S and I spins, respectively. Quality factors can be determined by, say, the B_e^J sideband intensity, and the frequency width of the sidebands at half height, and such quality factors can be used to judge the progressive improvement of probe designs or the effect of inhomogeneity on different pulse sequences. Thus this 1D method, as illustrated in Fig. 3, provides a quick means of comparing different sequences, different probes, and different probe manufacturers.

Uncertainties in the interpretation of the 1D spectra arising from the $\theta \sin\theta$ S-spin response can be eliminated by spatially imaging the signal via insertion of an incremented phase-encoding field gradient along the sample axis after the 90[S] pulse in any of COD1–3 (a spin-echo is not necessary if the S spins are on resonance). As illustrated by the scale in Fig. 3, the B_e^J frequency axis obtained from the FT of each FID along the

t_2 dimension can be converted to B_1, which is the desired RF amplitude from the probe, and the t_1 dimension provides the distance axis. Thus, the $\theta\sin^2\theta\sin^2\phi$ signal variation for COD2 (or $\theta\sin^n\theta\sin^m\phi$ in general) becomes a S/N contour plot as in Fig. 4a. However, for ideal probes producing single values of B_1 for each sample cross-section along the z axis, the S/N contours provide no additional information, since B_1 is given by the t_2 dimension. Results can then be displayed as simpler line plots using either the average B_1 across the contours or B_1 for the contour of maximum S/N, at each point in the sample. Figure 4a also shows a line plot for the results obtained for a ^{13}C coil in a high-resolution probe using COD2 or COD3 to detect the large ^{1}H signals from multiple quantum or antiphase coherence. The results in Fig. 4a were chosen to demonstrate that in this case the contour plot *does* contain more information than the line plot because the probe is not ideal: Whereas only single values of B_1 are apparent from the contours near the extremities of the coil at 5 and 20 mm, the S/N contours at the center of the coil show two B_1 values. Projecting the sum of the contours onto the RF axis gives the 1D spectrum of one of the sidebands, and thus the dip anomaly in the peaks in Fig. 3 also corresponds to these two dominant B_1 values. This anomaly could correspond to either an asymmetric or a concentric variation of B_1 across the sample's center, which can be determined by adding a second phase-encoding gradient along the x or y axis of the sample. Such 3D studies should allow the probe manufacturer to correlate the anomaly with an aspect of the probe design so that in future the simple 1D COD2 method of Fig. 3 could be used by the manufacturer or a customer to ensure quality control.

Although the ^{1}H coil can be characterized using COD4 or COD5 to detect the coherence signals via the ^{13}C spins as in Fig. 4b, a faster method is to directly detect the sensitive nucleus with better S/N using the established incremented-pulse technique (*10*), and comparative results are shown in Fig. 4c. However, one advantage of COD4/COD5, apparent from the preceding discussion, is that B_1 anomalies will usually be obvious from the quick 1D implementation of COD4/COD5 in the absence of field gradients, whereas the incremented-pulse method is minimally a 2D field-gradient technique. The comparison shown in Figs. 4b and 4c for the ^{1}H coil also serves to highlight the S/N advantage of COD2/COD3 for the reverse situation of the ^{13}C coil. The signal intensity contours in Fig. 4a, obtained in less than 10 min, revealed the source of the ^{13}C coil's B_1 anomaly observed in Fig. 3. The alternative lower S/N ^{13}C incremented-pulse method (results not shown) only vaguely indicated the same features after a 4-h experiment.

The excellent agreement between Fig. 4b and the established method of Fig. 4c confirms the validity and accuracy of our new techniques. Jahnke's (*15*) results, obtained by measuring 360° pulse times using tiny samples placed at calibrated distances along the sample axis, are plotted in Fig. 4d in good agreement with both methods.

The results in Figs. 1–4 demonstrate the value of the new COD pulse sequences for the characterization of heteronuclear probes. We have not yet explored the use of 90^J pulses generally for selective NMR but it is likely that $90^J[I]$ can take the place of any nonselective $\{(2J)^{-1}$–$90[I]\}$ part of any pulse sequence for an IS-spin system. Since a second $90^J[I]$ is equivalent to a selective $\{90[I]$–$(2J)^{-1}\}$ combination, and $90^J[I]$ can be mixed with $90^J[S]$, the number of possibilities multiply by four. We plan to address the uses and limitations of 90^J pulses for selective NMR, and their possible extension to I_mS_n systems, in future work.

REFERENCES

1. M. H. Levitt, G. Bodenhausen, and R. R. Ernst, *J. Magn. Reson.* **53,** 443 (1983).
2. M. R. Bendall and T. E. Skinner, *J. Magn. Reson.* **129,** 30 (1998).
3. M. R. Bendall, *J. Magn. Reson. A* **112,** 126 (1995).
4. T. E. Skinner and M. R. Bendall, *J. Magn. Reson.* **134,** 315 (1998).
5. R. R. Ernst, *J. Chem. Phys.* **45,** 3845 (1966).
6. K. G. R. Pachler, *J. Magn. Reson.* **7,** 442 (1972).
7. W. A. Anderson and R. Freeman, *J. Chem. Phys.* **37,** 85 (1962).
8. D. M. Thomas, M. R. Bendall, D. T. Pegg, D. M. Doddrell, and J. Field, *J. Magn. Reson.* **42,** 298 (1981).
9. A. Bax, *J. Magn. Reson.* **52,** 76 (1983); J. M. Bernassau, *J. Magn. Reson.* **62,** 533 (1985); N. Chandrakumar, *J. Magn. Reson.* **63,** 174 (1985).
10. S. L. Talagala and J. Gillen, *J. Magn. Reson.* **94,** 493 (1991).
11. J. S. Waugh, *J. Magn. Reson.* **49,** 517 (1982).
12. S. D. Simova, *J. Magn. Reson.* **63,** 583 (1985).
13. M. R. Bendall and R. E. Gordon, *J. Magn. Reson.* **53,** 365 (1983).
14. M. R. Bendall and D. T. Pegg, *J. Magn. Reson.* **57,** 337 (1984); *Magn. Reson. Med.* **2,** 91 (1985); **2,** 298 (1985).
15. W. Jahnke, *J. Magn. Reson. B* **113,** 262 (1996).